



# Worm-like S-doped RhNi alloys as highly efficient electrocatalysts for hydrogen evolution reaction



Jiajia Lu<sup>a</sup>, Zheng Tang<sup>b</sup>, Lin Luo<sup>a</sup>, Shibin Yin<sup>a,\*</sup>, Pei Kang Shen<sup>a</sup>, Panagiotis Tsiakaras<sup>c,d,e,\*</sup>

<sup>a</sup> Collaborative Innovation Center of Sustainable Energy Materials, Guangxi Key Laboratory of Electrochemical Energy Materials, College of Chemistry and Chemical Engineering, State Key Laboratory of Processing for Non-Ferrous Metal and Featured Materials, Guangxi University, Nanning, 530004, China.

<sup>b</sup> Hunan Provincial Key Laboratory of Chemical Power Sources, College of Chemistry and Chemical Engineering, Central South University, Changsha, 410083, China.

<sup>c</sup> Laboratory of Electrochemical Devices based on Solid Oxide Proton Electrolytes, Institute of High Temperature Electrochemistry, RAS, Yekaterinburg, 620990, Russia.

<sup>d</sup> Laboratory of Materials and Devices for Clean Energy, Ural Federal University, 19 Mira Street, Yekaterinburg, 620002, Russia.

<sup>e</sup> Laboratory of Alternative Energy Conversion Systems, Department of Mechanical Engineering, School of Engineering, University of Thessaly, Pedion Areos, 38834, Greece.

## ARTICLE INFO

### Keywords:

Worm-like  
RhNi alloy  
sulfur doping  
Electrocatalysts  
Hydrogen evolution reaction

## ABSTRACT

Precious metals are considered as the most efficient electrocatalysts for boosting the dynamic process of cathode in water electrolysis devices. Due to the large surface areas and the low coordination numbers of surface atoms, their one-dimensional ultrafine nanowires and two-dimensional ultrathin nanosheets are continually being investigated, while stacking problems inevitably affect their activities and stabilities.

We describe herein a three-dimensional metal network electrocatalyst consisting of a worm-like S-doped RhNi alloy (S-RhNi), which improves the performance for hydrogen evolution reaction (HER). Experimental results reveal that S-RhNi exhibits Pt-like HER activity with an onset potential close to 0 mV and a Tafel slope of 24.61 mV dec<sup>-1</sup> in 0.5 M H<sub>2</sub>SO<sub>4</sub> aqueous solution, having also good stability. The polarization curve shifts only 3.9 mV at a current density of  $-60 \text{ mA cm}^{-2}$  after 1,000 cycles and the potential displays a slight change after holding the current density at  $-20 \text{ mA cm}^{-2}$  for 10 h. This improved performance is supposed to be originated from the combination between the worm-like RhNi alloy, doped S atoms, and the three-dimensional structure. Overall, the results obtained and the facile synthesis methods offer a promising electrocatalyst for scaling-up hydrogen evolution.

## 1. Introduction

Due to the depletion and pollution issues associated with fossil fuels, sustainable power sources such as hydrogen, solar and wind power have attracted increasing attention [1–3]. Pure hydrogen with high energy densities and environment-friendly features can be efficiently obtained at the cathode of water electrolysis [4]. Currently, precious metals such as Pt [5–8], Rh [9–13], Ir [14–16], Ru [17–19] and Pd [20–22] are still considered as efficient electrocatalysts for HER, while the scarcity and high cost limit their large-scale applications [23]. Fortunately, some strategies such as ultrafine nanoparticles, alloy with nonprecious metals, and hybridization with heteroatoms, special morphologies and structures have been proposed and investigated for improving the utilization of precious metals.

As a member of the precious metals group, Rh exhibits promising activity for HER. Employing the aforementioned strategies alone or in combination with other metals can further enhance the catalytic performance for HER as well as reduce costs. As examples, ultrafine Rh<sub>2</sub>P

[24] and B-RhFe [25] nanoparticles, Rh nanowires [26], Rh<sub>2</sub>P nanocubes [27] and Rh-MoS<sub>2</sub> nanocomposites [28] have been reported. These electrocatalysts exhibited Pt-like activities for HER in acidic solutions [27] and some were even superior to Pt in alkaline solutions [24,25] because of the respective or combined advantages of these strategies. Ultrafine nanoparticles increase the surface area of the precious metals, thereby improving their utilization. Alternatively, alloying these precious metal atoms with nonprecious ones or hybridizing them with heteroatoms, modifies their electronic structures, which tunes the Gibbs free energy value of hydrogen adsorption of the electrocatalysts [24,25]. Special morphologies and structures can additionally uncover or generate more active sites [29]. Ultrathin nanosheets are widely studied, owing to the large surface areas and the low coordination numbers of surface atoms, where electrochemical reactions readily occur [30,31]. However, for all two-dimensional nanomaterials, a stacking problem inevitably affects the activity and stability of electrocatalysts. In order to reduce the unfavorable effects of stacking on catalytic performance, three-dimensional nanomaterials

\* Corresponding authors.

E-mail addresses: [yinshibin@gxu.edu.cn](mailto:yinshibin@gxu.edu.cn) (S. Yin), [tsiak@uth.gr](mailto:tsiak@uth.gr) (P. Tsiakaras).

with unique structural features and less Ostwald ripening/aggregation have been studied [32–34]. Chen and co-workers reported ultrathin rhodium oxide nanosheet nanoassemblies ( $\text{Rh}_2\text{O}_3\text{-NSNSs}$ ) electrocatalysts for oxygen evolution reaction. The authors found that the obtained  $\text{Rh}_2\text{O}_3\text{-NSNSs}$  presented good catalytic activity due to the combination of the ultrathin nanosheets and three-dimensional structural advantages [30].

Inspired by these ideas, in this work, we first report the synthesis of three-dimensional metal network electrocatalysts that are made up of the worm-like S-doped RhNi alloys (S-RhNi), which combines the advantages of alloying with nonprecious metals, doped heteroatoms, and special morphologies and structures for boosting the HER. During the electrochemical measurement, S-RhNi is mixed with XC-72 carbon that is referred to as S-RhNi/C, which possesses Pt-like catalytic activity for hydrogen evolution reaction in 0.5 M  $\text{H}_2\text{SO}_4$  aqueous solution, and also has good stability. The facile synthesis protocol coupled with its high performance offers a promising electrocatalyst for scalable hydrogen evolution.

## 2. Experimental

The S-RhNi synthesis procedure is schematically illustrated in Fig. 1.

### 2.1. Synthesis of S-RhNi, S-Rh and S-Ni

The worm-like S-RhNi was prepared as follows: 20 mL aqueous solutions including 5.0 mmol  $\text{L}^{-1}$   $\text{Rh}(\text{NO}_3)_3$  and 5.0 mmol  $\text{L}^{-1}$   $\text{H}_2\text{SO}_4$  were transferred into a 50 mL Teflon-lined stainless steel autoclave. A piece of Ni foil ( $1 \times 2 \text{ cm}^2$ ), cleaned by ultrasonication in deionized water and ethanol for 30 min each, was placed at the bottom of an autoclave. The autoclave was heated in an oven at 140 °C for 12 h. After cooling to room temperature, lemon yellow precipitates on the Ni foil were collected, centrifuged, and dried in vacuum at 50 °C for 12 h. Finally, the dried powders were heated at 300 °C for 2 h in a tube furnace under a continuous flow of  $\text{N}_2$ . Similarly, the S-doped Rh (S-Rh) was synthesized without using the Ni foils being placed in the autoclave. The S-doped Ni (S-Ni) was prepared without  $\text{Rh}(\text{NO}_3)_3$ .

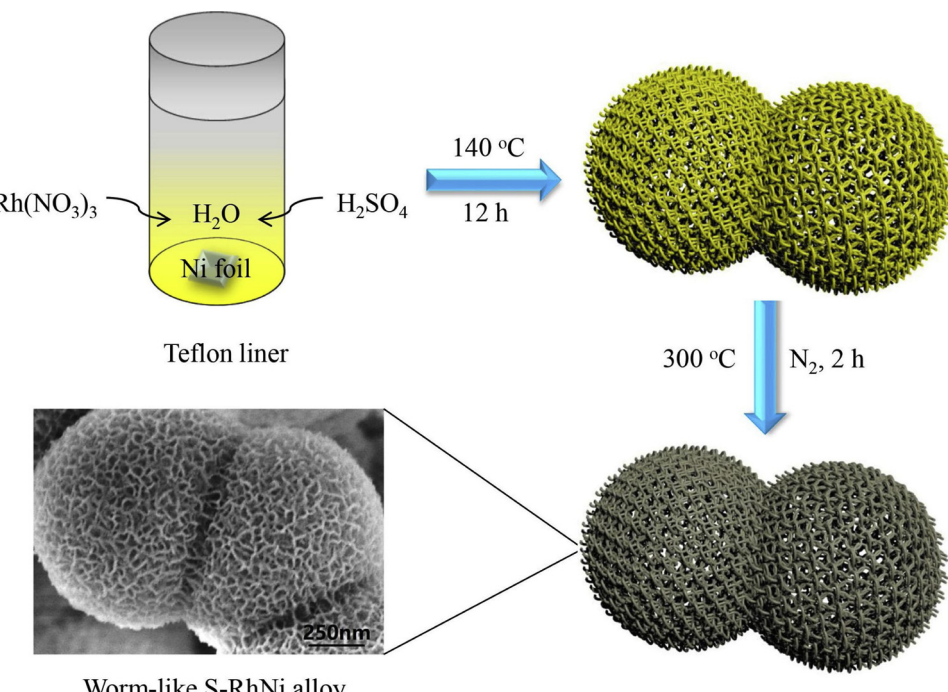


Fig. 1. Schematic diagram for the synthesis of the worm-like S-RhNi alloys.

### 2.2. Materials characterization

These samples were characterized by X-ray powder diffraction (SmartLab, Rigaku Co., Japan) equipped with  $\text{Cu Ka}$  radiation ( $\lambda = 0.15406 \text{ nm}$ ). The accelerating voltage, applied current, and scan rate were 40 kV, 30 mA, and  $5^\circ \text{ min}^{-1}$ , respectively. The surface morphology of the as prepared samples was characterized by the aid of field-emission scanning electron microscopy (FE-SEM SU8220, HITACHI, Japan).

An environmental spherical aberration corrected scanning transmission electron microscopy (Titan ETEM G2 80–300, FEI company, USA), operating at 300 kV, was used to characterize high resolution transmission electron microscopy (HRTEM) images and energy dispersive spectroscopy (EDS) of the prepared samples. X-ray photoelectron spectroscopy (XPS) was carried out on an ESCALAB-250i instrument (ThermoFisher, USA), using a monochromatic  $\text{Al K}\alpha$  radiation source. The specific surface area of substrates were carried out on an ASAP 2420 (Micromeritics Co., USA) by analysis of  $\text{N}_2$  adsorption/desorption data at 77 K.

### 2.3. Electrochemical tests

Electrochemical performances of electrocatalysts were evaluated on a Pine electrochemical station (Wavedrive20, USA) with a thermostatically-controlled standard three-electrode cell at 25 °C in 0.5 M  $\text{H}_2\text{SO}_4$  aqueous solution. A saturated calomel electrode and a carbon rod were served as the reference and counter electrode. All potentials were calibrated against the reversible hydrogen electrode [35], the only difference being in the sulfuric acid electrolyte instead of perchloric acid.

Preparation of the working electrode was as follows: 8.0 mg of XC-72 carbon and 2.0 mg of S-RhNi or S-Rh or S-Ni nanoparticles were added into 2.0 mL solution, which included 0.04 mL 5 wt% Nafion solution and 1.96 mL ethanol. After ultrasonication for about 30 min, 0.01 mL suspension was transferred onto a glassy carbon electrode (5 mm of diameter). The above samples were denoted as S-RhNi/C, S-Rh/C and S-Ni/C. The loadings of S-RhNi/C, S-Rh/C and S-Ni/C on glassy carbon electrode were 0.05 mg. For comparison, 0.05 mg of

commercial 20 wt% Pt/C electrocatalysts and 0.05 mg of XC-72 carbon were also evaluated by the glassy carbon electrode.

Polarization curves with a scan rate of  $5 \text{ mV s}^{-1}$  were conducted in  $\text{N}_2$ -saturated 0.5 M  $\text{H}_2\text{SO}_4$  aqueous solution at a rotating speed of 1,600 rpm. After initial activity, electrochemical stability was evaluated by polarization curves before and after 1,000 cycles between  $-0.1 \text{ V}$  and  $+0.1 \text{ V}$ , and a chronopotentiometry curve holding the current density at  $-20 \text{ mA cm}^{-2}$ . All polarization curves were presented with IR compensation.

Electrochemical impedance spectroscopy (EIS) measurements were conducted in a ZAHNER electrochemical station (ZAHNER IM6e, Germany). EIS patterns were recorded at different potentials with 5 mV amplitude in a frequency width from 100 kHz to 100 mHz in Fig. S5. Here, above  $R$  is replaced by the uncompensated ohmic series resistances  $R_s$ . The  $R_s$  of C, S-Ni/C, S-Rh/C, S-RhNi/C, and Pt/C were found to be 0.958, 1.001, 0.960, 1.095, and  $0.940 \Omega \text{ cm}^2$ , respectively.

### 3. Results and discussion

The worm-like S-RhNi alloy was synthesized by a hydrothermal method in a 50 mL Teflon-lined stainless steel autoclave with a piece of Ni foil,  $\text{Rh}(\text{NO}_3)_3$  and  $\text{H}_2\text{SO}_4$  aqueous solutions, followed by annealing at  $300^\circ\text{C}$  for 2 h in a tube furnace under a flow of  $\text{N}_2$ . For comparison, the S-Rh and the S-Ni were also prepared by a similar method omitting the Ni foils and without  $\text{Rh}(\text{NO}_3)_3$ , respectively. The morphology and composition of S-RhNi were first characterized by field-emission scanning electron microscopy (FE-SEM, Fig. 2).

The low-magnification SEM image of S-RhNi in Fig. 2a displays the chain-like spheres, while the high-magnification SEM image (Fig. 2b) shows that the sphere is composed of a worm-like S-RhNi alloy. The structure facilitates mass and charge transfer, improving thereby HER catalytic activity. However, the low- and high-magnification SEM

images of S-Rh merely display chain-like spheres [Figs S1(a–c)]. It indicates that the Ni foil plays a crucial role in the formation of the worm-like structures. The SEM images of S-Ni show sheet-like structures [Figs S3(a–c)]. Additionally, these elements in S-RhNi, S-Rh and S-Ni can be confirmed by energy dispersive spectroscopy (EDS) in Figs. 2c, S1(d–f) and S3(d–f).

The morphology and crystal structure of S-RhNi were further characterized by transmission electron microscopy (TEM). Fig. 3a shows chain-like spheres as presented in Fig. 2a and the worm-like structures (Fig. 2b) are also detected at the edge of the sphere in Fig. 3b. Crystal lattice information about S-RhNi is investigated by high-resolution TEM (HRTEM, Fig. 3c and d). The highlighted lattice distances of 0.2086, 0.2092 and 0.2108 nm correspond to the (111) facets of Ni (PDF#87-0712) named as NiRh(111) in Fig. 3c and d. Compared to the standard lattice distance (0.2035 nm) of the (111) facets of Ni (PDF#87-0712), the relatively larger lattice distances could be attributed to the larger atomic radius of Rh embedded in the Ni lattice, resulting in a tensile lattice strain. Moreover, a lattice distance of 0.2176 nm corresponds to the (111) facets of Rh (PDF#05-0685), which is referred to as RhNi(111) in Fig. 3c and d. The lattice distance is smaller than that of the standard (111) facets of Rh (0.2196 nm) (PDF#05-0685), owing to the smaller atomic radius of Ni that causes a contraction of the Rh lattice. Fig. 3e displays the high angle annular dark field scanning transmission electron microscopy (HAADF-STEM) image and the EDS elemental mapping images of S-RhNi, where can be distinguished that the Rh, Ni and S atoms are homogeneously distributed.

The RhNi alloy phase can be further demonstrated by X-ray diffraction (XRD) in Fig. 4a, since the diffraction peaks of S-RhNi are found between Rh (PDF#05-0685) and Ni (PDF#87-0712). This result is consistent with the findings of the HRTEM. For S-Rh, the observed diffraction peaks are reflecting to Rh (PDF#05-0685). As shown in Fig.

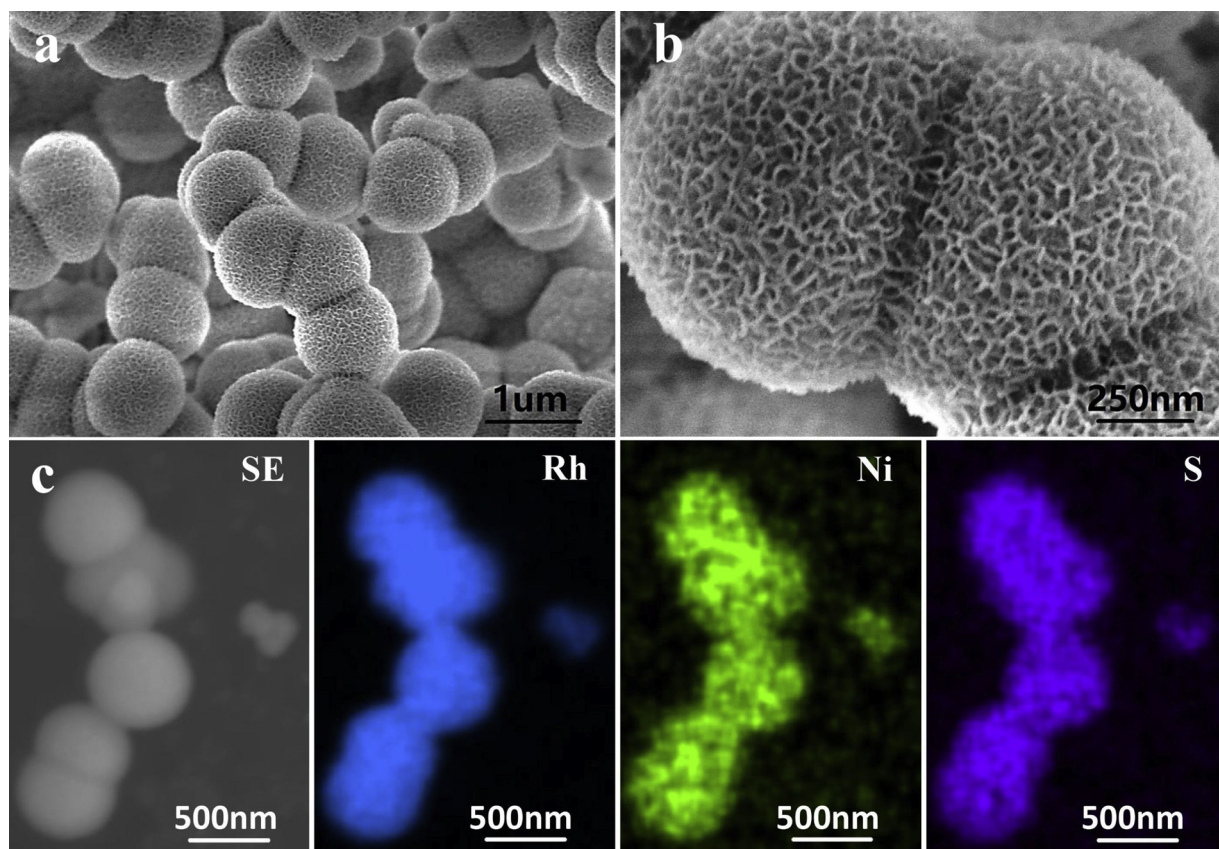


Fig. 2. a) The low- and b) high-magnification SEM images of S-RhNi. c) The corresponding EDS elemental mapping images of Rh, Ni, and S.

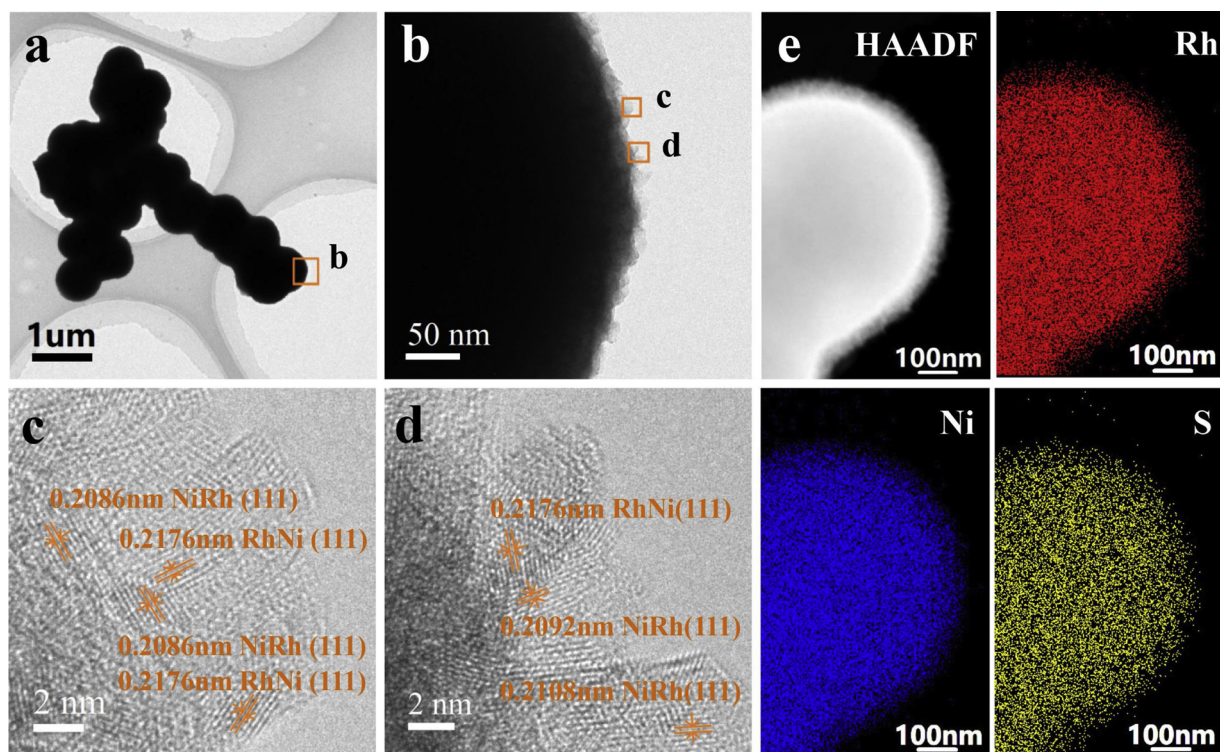


Fig. 3. a) and b) TEM images of S-RhNi. c) and d) The HRTEM images of b. e) HAADF-STEM and EDS elemental mapping images of S-RhNi.

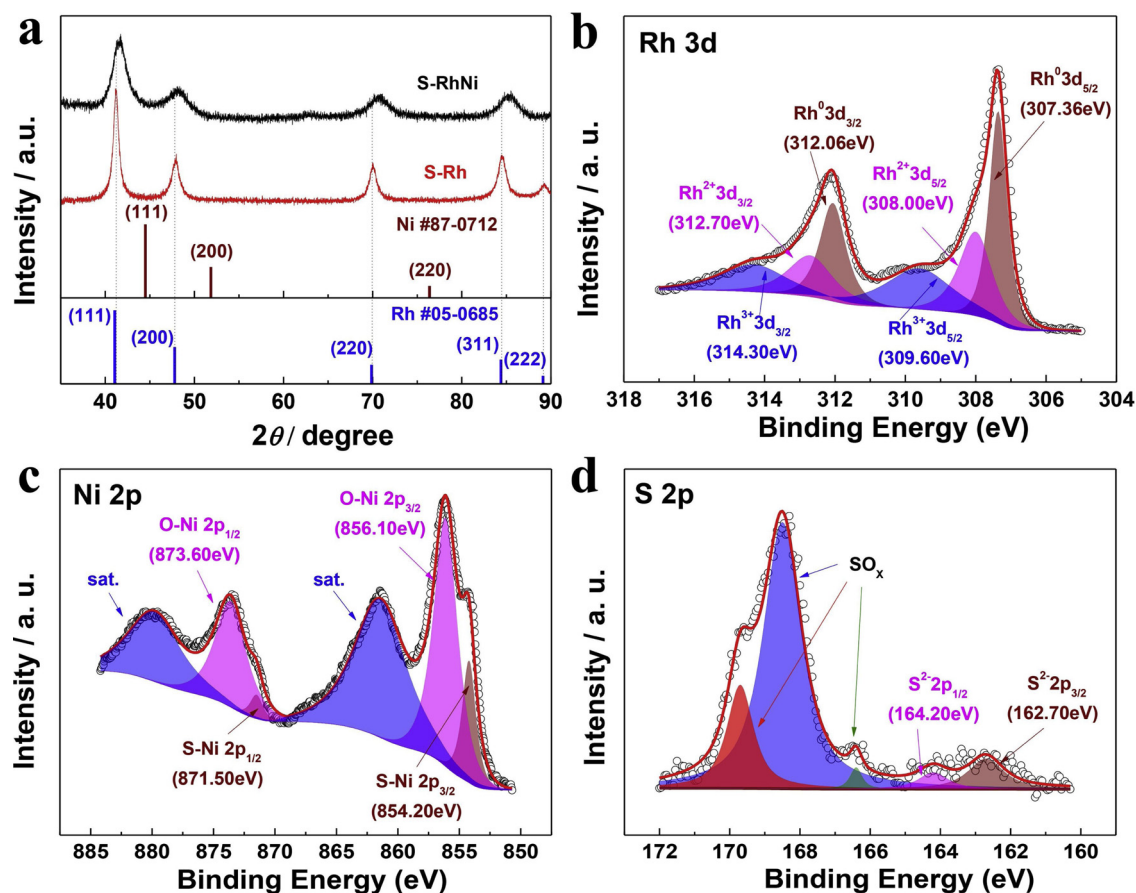


Fig. 4. a) XRD patterns of S-RhNi and S-Rh. High-resolution XPS spectra of Rh3d (b), Ni2p (c), and S2p (d) for S-RhNi.

S4, the diffraction peaks of S-Ni correspond to NiO (PDF#89-7130) and three strong diffraction peaks are assigned to Ni foils because similar diffraction peaks are found in pure Ni foils. The elemental chemical compositions of S-RhNi and their valence states elucidated by X-ray photoelectron spectroscopy results are displayed in Fig. 4(b-d), and the contents of these elements are shown in Table S1. More precisely, Fig. 4b displays six overlapping spectra of Rh. Peaks located at 307.36, 308.00, 309.60, 312.06, 312.70 and 314.30 eV may be assigned to  $\text{Rh}^0\text{3d}_{5/2}$ ,  $\text{Rh}^{2+}\text{3d}_{5/2}$ ,  $\text{Rh}^{3+}\text{3d}_{5/2}$ ,  $\text{Rh}^0\text{3d}_{3/2}$ ,  $\text{Rh}^{2+}\text{3d}_{3/2}$  and  $\text{Rh}^{3+}\text{3d}_{3/2}$ , respectively. Compared with the  $\text{3d}_{5/2}$  peak (307.0 eV) of metallic Rh, the binding energy of  $\text{Rh}^0\text{3d}_{5/2}$  in S-RhNi is more positive, which indicates that the Rh in S-RhNi possesses a small positive charge [24]. This could be explained by the effect of the adjacent oxygen or sulfur atoms that have stronger electronegativity than Rh atoms. And the Ni in S-RhNi mainly exists in the form of the oxidized species (Fig. 4c). The peak located at the lower binding energy may be the S-Ni bonds because of the weaker electronegativity of sulfur compared to oxygen [36]. Moreover, S in S-RhNi is presented in the form of  $\text{SO}_x$  and  $\text{S}^{2-}$  [37]. The  $\text{SO}_x$  could be due to the sulfate anion in the hydrothermal system and the  $\text{S}^{2-}$  may form compounds with Rh or Ni, modifying the electronic structure of these metals and thereby facilitating the reaction of hydrogen evolution. Besides, the sulfate anion plays a crucial role in the formation of the worm-like structures because the lemon yellow precipitates were not found without sulfate anion in aqueous solution.

To evaluate the HER performance of the electrocatalysts, S-RhNi, S-Rh and S-Ni were mixed with XC-72 carbon, and denoted as S-RhNi/C, S-Rh/C and S-Ni/C. All electrochemical tests were conducted in a 0.5 M  $\text{H}_2\text{SO}_4$  aqueous solution by employing a thermostatically-controlled standard three-electrode cell, operating at 25 °C. As observed in Fig. 5a, the S-RhNi/C exhibits the best catalytic activity (Pt-like) for HER among all the tested electrocatalysts with an onset potential close to 0 mV and a small overpotential of 41.78 mV at a current density of

$-60 \text{ mA cm}^{-2}$ , which is even slightly lower than the overpotential (44.75 mV) required of the commercial Pt/C to reach the same current density. The S-Rh/C shows an onset potential of  $-12.43 \text{ mV}$  and a clearly larger overpotential of  $109.32 \text{ mV}$  at a current density of  $-60 \text{ mA cm}^{-2}$ . This behavior clearly implies that Ni plays an important role, not only in forming the worm-like structures but also in improving HER activity. The S-Ni/C displays a more negative onset potential (about  $-100 \text{ mV}$ ) and the largest overpotential ( $> 400 \text{ mV}$ ) at a current density of  $-60 \text{ mA cm}^{-2}$ . Furthermore, in order to eliminate the influence of the XC-72 carbon in S-RhNi/C, S-Rh/C and S-Ni/C, pure XC-72 (denoted as C in Fig. 5a) was also tested and clearly demonstrated to display negligible catalytic activity for hydrogen evolution. The mass activities for all the electrocatalysts (the mass vs C, S-Ni, S-Rh, S-RhNi and Pt) were evaluated in Fig. S6. A similar trend is found and a possible explanation is that the same mass of active substances (S-Ni, S-Rh, S-RhNi and Pt) is investigated on glass carbon electrodes.

The Tafel slope, which reflects the reaction mechanism is another important parameter to evaluate the HER catalytic activity of electrocatalysts. This value derives from the Tafel plots obtained from EIS curves (Fig. S5) by plotting the reciprocal of the  $R_{\text{ct}}$  versus potential [ $\log(1/R_{\text{ct}})$  vs  $E$ ], as shown in Fig. 5b. Notably, the Tafel slope of S-RhNi/C is  $24.61 \text{ mV dec}^{-1}$ , which is even lower than that of commercial Pt/C ( $25.88 \text{ mV dec}^{-1}$ ). This result proves the kinetic favorability of S-RhNi/C toward HER in acidic solutions and indicates that S-RhNi/C undergoes the Volmer-Tafel mechanism, where a chemical desorption process of hydrogen (Tafel step) is the rate-limiting step [38]. Compared with S-RhNi/C, S-Rh/C shows a Tafel slope of  $45.94 \text{ mV dec}^{-1}$ , which follows the Volmer-Heyrovsky mechanism in HER processes in which the electrochemical desorption of hydrogen (Heyrovsky step) dominates the whole reaction [39]. For S-Ni/C ( $219.13 \text{ mV dec}^{-1}$ ), the adsorption of hydrogen (Volmer step) could be the rate-determining process. Comparisons of HER activities for all the as-tested electrocatalysts,

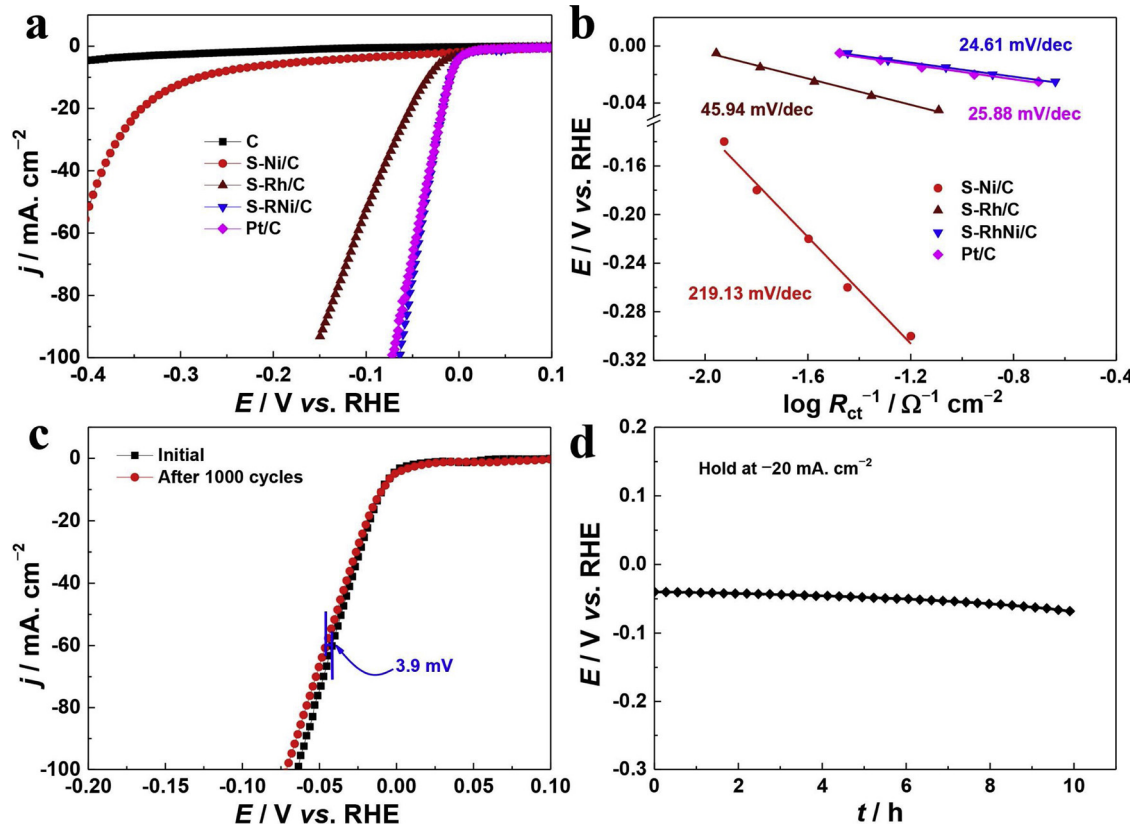


Fig. 5. a) Polarization curves with IR compensation of C, S-Ni/C, S-Rh/C, S-RhNi/C, and Pt/C in 0.5 M  $\text{H}_2\text{SO}_4$  aqueous solution. b) The Tafel plots of S-Ni/C, S-Rh/C, S-RhNi/C, and Pt/C. c) Polarization curves of S-RhNi/C initially and after 1,000 cycles, between  $-0.1 \text{ V}$  and  $+0.1 \text{ V}$ . d) Chronopotentiometry curve of S-RhNi/C at the current density of  $-20 \text{ mA cm}^{-2}$  for 10 h.

**Table 1**

Comparisons of HER activities for all the as-prepared electrocatalysts except C.

	$\eta_{\text{onset}}^{\text{a}}$ [mV]	$\eta_{20}^{\text{b}}$ [mV]	$\eta_{60}^{\text{c}}$ [mV]	$b^{\text{d}}$ [mV dec $^{-1}$ ]
S-Ni/C	-100	342.73	> 400	219.13
S-Rh/C	-12.43	51.83	109.32	45.94
S-RhNi/C	0	17.33	41.78	24.61
Pt/C	0	17.49	44.75	25.88

<sup>a</sup> Onset potential.<sup>b</sup> Overpotential at the current density of -20 mA cm $^{-2}$ .<sup>c</sup> Overpotential at the current density of -60 mA cm $^{-2}$ .<sup>d</sup> Tafel slope.

except for C, are summarized in **Table 1**. Furthermore, we evaluated the amount of H<sub>2</sub> production theoretically calculated and actually measured at the current of 5.0 mA *versus* time for S-RhNi/C in 0.5 M H<sub>2</sub>SO<sub>4</sub> aqueous solution; the results are shown in Fig. S7. The amount of H<sub>2</sub> evolved at the current of 5.0 mA agrees with the theoretical value, suggesting a Faradaic efficiency close 100%. The outstanding HER activity for S-RhNi/C could be due to the following reasons: i) the Ni in RhNi alloy modifies the electronic structure of Rh, which could be in favor of hydrogen evolution reaction [40,41], additionally, considering that the Ni that has a lower Gibbs free energy value for hydrogen adsorption than Rh is advantageous to increase the hydrogen coverage and further enhance HER activity [42,43]; ii) the S<sup>2-</sup> obtained from XPS may form compounds with Rh or Ni, optimizing the electronic structure of these metals and thereby enhancing their catalytic activity [44–46]; iii) the three-dimensional metal network is conducive to the mass and charge transfers [47] and avoids the stacking problem of electrocatalysts observed in one- or two-dimensional structures, and iv) the worm-like structure (S-RhNi) has larger specific surface area (Table S2), analyzed by N<sub>2</sub> adsorption/desorption data at 77 K (Fig. S8), than the sphere-like structure (S-Rh) and the sheet-like structure (S-Ni).

It is well known that stability is a significant criterion to judge HER performance of electrocatalysts. Two kinds of methods: i) continuous cyclic voltammetry (CV) and ii) chronopotentiometry (CP), were investigated here, using an aqueous solution containing 0.5 M H<sub>2</sub>SO<sub>4</sub>. **Fig. 5c** illustrates that the polarization curve of S-RhNi/C only shifts 3.9 mV at a current density of -60 mA cm $^{-2}$  after 1,000 cycles between -0.1 and +0.1 V, indicating good stability. Furthermore, the potential exhibits a slight change after holding the current density at -20 mA cm $^{-2}$  for 10 h (**Fig. 5d**).

The slight degradation of HER performances could be ascribed to the following reasons: i) nickel or nickel oxides on the surface of electrocatalysts are inevitably dissolved because the main component of worms is Ni (confirmed by the XPS spectra in Table S1) and S-RhNi/C is operated in a strong acidic electrolyte, and ii) from the SEM images of S-RhNi/C after holding the current density at -20 mA cm $^{-2}$  for 10 h in **Fig. S2**, a slight degradation of dendrites in a three-dimensional metal network is noticed, which would decrease the active sites for boosting the catalytic activity for hydrogen evolution reaction.

#### 4. Conclusions

In summary, a three-dimensional metal network electrocatalyst composed of a worm-like S-doped RhNi alloy has been successfully synthesized by a hydrothermal method followed by annealing in high temperature. Benefiting from the combination of the worm-like RhNi alloy, doped S atoms, and the three-dimensional structure, the S-RhNi/C shows Pt-like HER activity regarding its Tafel slope and overpotentials at the current density of -20 and -60 mA cm $^{-2}$  in 0.5 M H<sub>2</sub>SO<sub>4</sub> aqueous solution. Furthermore, it also exhibits good stability after 1,000 cycles or holding the current density at -20 mA cm $^{-2}$  for 10 h. More importantly, this study provides a way for producing novel electrocatalysts, aiming at enhancing HER performance and reducing costs by combining the advantages of different strategies for improving

the utilization of precious metals.

#### Acknowledgements

This work was supported by the Natural Science Foundation of China (21872040), the Natural Science Foundation of Guangxi (2016GXNSFCB380002), and the Nanning Science and Technology Project (AB16380030). The Prof. Tsiakaras was co-financed by the European Union and Greek national funds through the Operational Program Competitiveness, Entrepreneurship and Innovation, under the call RESEARCH-CREATE-INNOVATE (project code:T1EDK-02442).

#### Appendix A. Supplementary data

Supplementary material related to this article can be found, in the online version, at doi:<https://doi.org/10.1016/j.apcatb.2019.05.039>.

#### References

- [1] A.P. Murthy, J. Madhavan, K. Murugan, Recent advances in hydrogen evolution reaction catalysts on carbon/carbon-based supports in acid media, *J. Power Sources* 398 (2018) 9–26, <https://doi.org/10.1016/j.jpowsour.2018.07.040>.
- [2] Y. Fu, H.Y. Yu, C. Jiang, T.H. Zhang, R. Zhan, X.W. Li, J.F. Li, J.H. Tian, R.Z. Yang, NiCo alloy nanoparticles decorated on N-doped carbon nanofibers as highly active and durable oxygen electrocatalyst, *Adv. Funct. Mater.* 28 (2018) 1705094, <https://doi.org/10.1002/adfm.201705094>.
- [3] C. Yu, J.J. Lu, L. Luo, F. Xu, P.K. Shen, P. Tsiakaras, S.B. Yin, Bifunctional catalysts for overall water splitting: CoNi oxyhydroxide nanosheets electrodeposited on titanium sheets, *Electrochim. Acta* 301 (2019) 449–457, <https://doi.org/10.1016/j.electacta.2019.01.149>.
- [4] S.Y. Jing, D.R. Wang, S.B. Yin, J.J. Lu, P.K. Shen, P. Tsiakaras, P-doped CNTs encapsulated nickel hybrids with flower-like structure as efficient catalysts for hydrogen evolution reaction, *Electrochim. Acta* 298 (2019) 142–149, <https://doi.org/10.1016/j.electacta.2018.12.055>.
- [5] P.T. Wang, K.Z. Jiang, G.M. Wang, J.L. Yao, X.Q. Huang, Phase and interface engineering of platinum-nickel nanowires for efficient electrochemical hydrogen evolution, *Angew. Chem. Int. Ed.* 55 (2016) 12859–12863, <https://doi.org/10.1002/anie.201606290>.
- [6] S. Chakrabarty, C.S. Gopinath, C.R. Raj, Polymer-based hybrid catalyst of low Pt content for electrochemical hydrogen evolution, *Int. J. Hydrogen Energy* 42 (2017) 22821–22829, <https://doi.org/10.1016/j.ijhydene.2017.07.152>.
- [7] Y.J. Li, H.C. Zhang, T.H. Xu, Z.Y. Lu, X.C. Wu, P.B. Wan, X.M. Sun, L. Jiang, Underwater superaerobic pine-shaped Pt nanoarray electrode for ultrahigh-performance hydrogen evolution, *Adv. Funct. Mater.* 25 (2015) 1737–1744, <https://doi.org/10.1002/adfm.201404250>.
- [8] S.H. Ahn, S.J. Yoo, H.J. Kim, D. Henkensmeier, S.W. Nam, S.K. Kim, J.H. Jang, Anion exchange membrane water electrolyzer with an ultra-low loading of Pt-decorated Ni electrocatalyst, *Appl. Catal. B* 180 (2016) 674–679, <https://doi.org/10.1016/j.apcatb.2015.07.020>.
- [9] J.J. Lu, L.S. Zhang, S.Y. Jing, L. Luo, S.B. Yin, Remarkably efficient PtRh alloyed with nanoscale WC for hydrogen evolution in alkaline solution, *Int. J. Hydrogen Energy* 42 (2017) 5993–5999, <https://doi.org/10.1016/j.ijhydene.2017.01.181>.
- [10] N. Singh, M. Gordon, H. Metiu, E. McFarland, Doped rhodium sulfide and thiospinels hydrogen evolution and oxidation electrocatalysts in strong acid electrolytes, *J. Appl. Electrochem.* 46 (2016) 497–503, <https://doi.org/10.1007/s10800-016-0938-0>.
- [11] J. Du, X.L. Wang, C. Li, X.Y. Liu, L. Gu, H.P. Liang, Hollow Rh nanoparticles with nanoporous shell as efficient electrocatalyst for hydrogen evolution reaction, *Electrochim. Acta* 282 (2018) 853–859, <https://doi.org/10.1016/j.electacta.2018.06.126>.
- [12] I. Golvano Escobal, S. Surinach, M. Dolors Baro, S. Pane, J. Sort, E. Pellicer, Electrodeposition of sizeable and compositionally tunable rhodium-iron nanoparticles and their activity toward hydrogen evolution reaction, *Electrochim. Acta* 194 (2016) 263–275, <https://doi.org/10.1016/j.electacta.2016.02.112>.
- [13] M.D. Sharma, C. Mahala, M. Basu, Nanosheets of MoSe<sub>2</sub>@M (M = Pd and Rh) function as widespread pH tolerable hydrogen evolution catalyst, *J. Colloid Interface Sci.* 534 (2019) 131–141, <https://doi.org/10.1016/j.jcis.2018.09.018>.
- [14] Y.C. Pi, Q. Shao, P.T. Wang, J. Guo, X.Q. Huang, General formation of monodisperse IrM (M = Ni, Co, Fe) bimetallic nanoclusters as bifunctional electrocatalysts for acidic overall water splitting, *Adv. Funct. Mater.* 27 (2017) 1700886, <https://doi.org/10.1002/adfm.201700886>.
- [15] K.A. Kuttiyiel, K. Sasaki, W.F. Chen, D. Su, R.R. Adzic, Core-shell, hollow-structured iridium-nickel nitride nanoparticles for the hydrogen evolution reaction, *J. Mater. Chem. A* 2 (2014) 591–594, <https://doi.org/10.1039/c3ta4301e>.
- [16] M. Duca, E. Guerrini, A. Colombo, S. Trasatti, Activation of nickel for hydrogen evolution by spontaneous deposition of iridium, *Electrocatalysis* 4 (2013) 338–345, <https://doi.org/10.1007/s12678-013-0148-z>.
- [17] C.L. Xu, M. Ming, Q. Wang, C. Yang, G.Y. Fan, Y. Wang, D.J. Gao, J. Bi, Y. Zhang, Facile synthesis of effective Ru nanoparticles on carbon by adsorption-low temperature pyrolysis strategy for hydrogen evolution, *J. Mater. Chem. A* 6 (2018)

14380–14386, <https://doi.org/10.1039/c8ta03572e>.

[18] F. Li, G.F. Han, H.J. Noh, I. Ahmad, I.Y. Jeon, J.B. Baek, Mechanochemically assisted synthesis of a Ru catalyst for hydrogen evolution with performance superior to Pt in both acidic and alkaline media, *Adv. Mater.* (2018) 1803676, , <https://doi.org/10.1002/adma.201803676>.

[19] Y.B. Cho, A. Yu, C. Lee, M.H. Kim, Y. Lee, Fundamental study of facile and stable hydrogen evolution reaction at electrospun Ir and Ru mixed oxide nanofibers, *ACS Appl. Mater. Interfaces* 10 (2018) 541–549, <https://doi.org/10.1021/acsami.7b14399>.

[20] S. Ghasemi, S.R. Hosseini, S. Nabipour, P. Asen, Palladium nanoparticles supported on graphene as an efficient electrocatalyst for hydrogen evolution reaction, *Int. J. Hydrogen Energy* 40 (2015) 16184–16191, <https://doi.org/10.1016/j.ijhydene.2015.09.114>.

[21] S.L. Liu, H. Zhang, X.Q. Mu, C.Y. Chen, Surface reconstruction engineering of twinned  $Pd_2CoAg$  nanocrystals by atomic vacancy inducement for hydrogen evolution and oxygen reduction reactions, *Appl. Catal. B* 241 (2019) 424–429, <https://doi.org/10.1016/j.apcatb.2018.09.067>.

[22] A. Doner, F. Tezcan, G. Kardas, Electrocatalytic behavior of the Pd-modified electrocatalyst for hydrogen evolution, *Int. J. Hydrogen Energy* 38 (2013) 3881–3888, <https://doi.org/10.1016/j.ijhydene.2013.01.141>.

[23] F. Xu, J.J. Lu, L. Luo, C. Yu, Z. Tang, H.S. Abbo, S.J.J. Titinchi, J.L. Zhu, P.K. Shen, S.B. Yin,  $Cu_2S-Cu_3P$  nanowire arrays self-supported on copper foam as boosting electrocatalysts for hydrogen evolution, *Energy Technol.* 7 (2019), <https://doi.org/10.1002/ente.201800993> 1800993.

[24] F.L. Yang, Y.M. Zhao, Y.S. Du, Y.T. Chen, G.Z. Cheng, S.L. Chen, W. Luo, A monodisperse  $Rh_2P$ -based electrocatalyst for highly efficient and pH-universal hydrogen evolution reaction, *Adv. Energy Mater.* 8 (2018) 1703489, , <https://doi.org/10.1002/aenm.201703489>.

[25] L.S. Zhang, J.J. Lu, S.B. Yin, L. Luo, S.Y. Jing, A. Brouzgou, J.H. Chen, P.K. Shen, P. Tsakarais, One-pot synthesized boron-doped  $Rh/Fe$  alloy with enhanced catalytic performance for hydrogen evolution reaction, *Appl. Catal. B* 230 (2018) 58–64, <https://doi.org/10.1016/j.apcatb.2018.02.034>.

[26] L.Q. Zhang, L.C. Liu, H.D. Wang, H.X. Shen, Q. Cheng, C. Yan, S. Park, Electrodeposition of rhodium nanowires arrays and their morphology-dependent hydrogen evolution activity, *Nanomaterials* 7 (2017) 103, <https://doi.org/10.3390/nano7050103>.

[27] H.H. Duan, D.G. Li, Y. Tang, Y. He, S.F. Ji, R.Y. Wang, H.F. Lv, P.P. Lopes, A.P. Paulikas, H. Li, S.X. Mao, C.M. Wang, N.M. Markovic, J. Li, V.R. Stamenkovic, Y.D. Li, High-performance  $Rh_2P$  electrocatalyst for efficient water splitting, *J. Am. Chem. Soc.* 139 (2017) 5494–5502, <https://doi.org/10.1021/jacs.7b01376>.

[28] Y.F. Cheng, S.K. Lu, F. Liao, L.B. Liu, Y.Q. Li, M.W. Shao, Rh- $MoS_2$  nanocomposite catalysts with Pt-like activity for hydrogen evolution reaction, *Adv. Funct. Mater.* 27 (2017) 1700359, , <https://doi.org/10.1002/adfm.201700359>.

[29] Z.H. Sun, X.C. Cao, I.G.G. Martinez, M.H. Rummeli, R.Z. Yang, Enhanced electrocatalytic activity of  $FeCo_2O_4$  interfacing with  $CeO_2$  for oxygen reduction and evolution reactions, *Electrochim. Commun.* 93 (2018) 35–38, <https://doi.org/10.1016/j.elecom.2018.06.001>.

[30] J. Bai, S.H. Han, R.L. Peng, J.H. Zeng, J.X. Jiang, Y. Chen, Ultrathin rhodium oxide nanosheet nanoassemblies: synthesis, morphological stability, and electrocatalytic application, *ACS appl. Mater. Interfaces* 9 (2017) 17196–17201, <https://doi.org/10.1021/acsami.7b04874>.

[31] H.H. Duan, N. Yan, R. Yu, C.R. Chang, G. Zhou, H.S. Hu, H.P. Rong, Z.Q. Niu, J.J. Mao, H. Asakura, T. Tanaka, P.J. Dyson, J. Li, Y.D. Li, Ultrathin rhodium nanosheets, *Nat. Commun.* 5 (2014) 3093, <https://doi.org/10.1038/ncomms4093>.

[32] B.Y. Xia, N. Wan Theng, H.B. Wu, X. Wang, X.W. Lou, Self-supported interconnected Pt nanoassemblies as highly stable electrocatalysts for low-temperature fuel cells, *Angew. Chem. Int. Ed.* 51 (2012) 7213–7216, <https://doi.org/10.1002/anie.201201553>.

[33] J. Bai, G.R. Xu, S.H. Xing, J.H. Zeng, J.X. Jiang, Y. Chen, Hydrothermal synthesis and catalytic application of ultrathin rhodium nanosheet nanoassemblies, *ACS Appl. Mater. Interfaces* 8 (2016) 33635–33641, <https://doi.org/10.1021/acsami.6b11210>.

[34] N. Zhang, Q. Shao, Y. Pi, J. Guo, X.Q. Huang, Solvent-mediated shape tuning of well-defined rhodium nanocrystals for efficient electrochemical water splitting, *Chem. Mater.* 29 (2017) 5009–5015, <https://doi.org/10.1021/acs.chemmater.7b01588>.

[35] S.Y. Jing, L. Luo, S.B. Yin, F. Huang, Y. Jia, Y. Wei, Z.H. Sun, Y.M. Zhao, Tungsten nitride decorated carbon nanotubes hybrid as efficient catalyst supports for oxygen reduction reaction, *Appl. Catal. B* 147 (2014) 897–903, <https://doi.org/10.1016/j.apcatb.2013.10.026>.

[36] C.Q. Wang, B. Tian, M. Wu, J.H. Wang, Revelation of the excellent intrinsic activity of  $MoS_2$  vertical bar NiS vertical bar  $MoO_3$  nanowires for hydrogen evolution reaction in alkaline medium, *ACS Appl. Mater. Interfaces* 9 (2017) 7084–7090, <https://doi.org/10.1021/acsami.6b14827>.

[37] K.Y. Tao, Y. Gong, J.H. Lin, Low-temperature synthesis of NiS/ $MoS_2/C$  nanowires/nanoflakes as electrocatalyst for hydrogen evolution reaction in alkaline medium via calcining/sulfurizing metal-organic frameworks, *Electrochim. Acta* 274 (2018) 74–83, <https://doi.org/10.1016/j.electacta.2018.04.090>.

[38] S.Y. Jing, J.J. Lu, G.T. Yu, S.B. Yin, L. Luo, Z.S. Zhang, Y.F. Ma, W. Chen, P.K. Shen, Carbon-encapsulated  $WO_3$  hybrids as efficient catalysts for hydrogen evolution, *Adv. Mater.* 30 (2018) 1705979, , <https://doi.org/10.1002/adma.201705979>.

[39] S.Y. Jing, L.S. Zhang, L. Luo, J.J. Lu, S.B. Yin, P.K. Shen, P. Tsakarais, N-doped porous molybdenum carbide nanobelts as efficient catalysts for hydrogen evolution reaction, *Appl. Catal. B* 224 (2018) 533–540, <https://doi.org/10.1016/j.apcatb.2017.10.025>.

[40] Z.J. Zhang, S.L. Zhang, Q.L. Yao, G. Feng, M.H. Zhu, Z.H. Lu, Metal-organic framework immobilized  $RhNi$  alloy nanoparticles for complete  $H_2$  evolution from hydrazine borane and hydrous hydrazine, *Inorg. Chem. Front.* 5 (2018) 370–377, <https://doi.org/10.1039/c7qi00555e>.

[41] A.K. Singh, Q. Xu, Synergistic catalysis over bimetallic alloy nanoparticles, *ChemCatChem* 5 (2013) 652–676, <https://doi.org/10.1002/cctc.201200591>.

[42] J.K. Norskov, T. Bligaard, A. Logadottir, J.R. Kitchin, J.G. Chen, S. Pandelov, J.K. Norskov, Trends in the exchange current for hydrogen evolution, *J. Electrochem. Soc.* 152 (2005) J23–J26, <https://doi.org/10.1149/1.1856988>.

[43] J.J. Lu, S.B. Yin, P.K. Shen, Carbon-encapsulated electrocatalysts for the hydrogen evolution reaction, *Electrochim. Energy Rev.* 2 (2019) 105–127, <https://doi.org/10.1007/s41918-018-0025-9>.

[44] D.Y. Chung, J.W. Han, D.H. Lim, J.H. Jo, S.J. Yoo, H. Lee, Y.E. Sung, Structure dependent active sites of  $Ni_3S_2$  as electrocatalysts for hydrogen evolution reaction, *Nanoscale* 7 (2015) 5157–5163, <https://doi.org/10.1039/c4nr07648f>.

[45] P. Luo, H.J. Zhang, L. Liu, Y. Zhang, J. Deng, C.H. Xu, N. Hu, Y. Wang, Targeted synthesis of unique nickel sulfide ( $NiS$ ,  $NiS_2$ ) microarchitectures and the applications for the enhanced water splitting system, *ACS Appl. Mater. Interfaces* 9 (2017) 2500–2508, <https://doi.org/10.1021/acsami.6b13984>.

[46] J. Masud, N. Trung Van, N. Singh, E. McFarland, M. Ikenberry, K. Hohn, C.J. Pan, B.J. Hwang, A  $Rh_xS_y/C$  catalyst for the hydrogen oxidation and hydrogen evolution reactions in HBr, *J. Electrochem. Soc.* 162 (2015) F455–F462, <https://doi.org/10.1149/2.0901504jes>.

[47] S.P. Luo, P.K. Shen, Concave platinum-copper octopod nanoframes bounded with multiple high index facets for efficient electrooxidation catalysis, *ACS Nano* 11 (2017) 11946–11953, <https://doi.org/10.1021/acsnano.6b04458>.